PAPER

Check for updates

Rugby ball-shaped magnetic microcapsule for tumor hyperthermia†

Siyao Wang,[a] Nana Wen,[a] Bin Yan,[a] Xuan Wang,[a] Zhiye Cai,[a] Yao Li[*b] and Xiaoli Liu [ID] [*acd]

Magnetic hyperthermia (MH) induced by magnetic particles has been widely used to treat tumors. However, the limited heating conversion efficiency inspires the design and synthesis of versatile magnetic materials for enhancing the performance of MH. Herein, we developed rugby ball-shaped magnetic microcapsules as efficient MH agents. The size and shape of the microcapsules can be precisely controlled by adjusting the reaction time and temperature without surfactant assistance. Because of their high saturation magnetization and uniform size/morphology, the microcapsules showed excellent thermal conversion efficiency, with a specific absorption rate of 2391 W g^{-1}. Additionally, we performed *in vivo* anti-tumor studies on mice and found that MH mediated by magnetic microcapsules effectively inhibited the advancement of hepatocellular carcinoma. The microcapsules' porous structure might allow them to efficiently load different therapeutic drugs and/or functional species. These beneficial properties make microcapsules ideal candidates for medical applications, particularly in disease therapy and tissue engineering.

1. Introduction

Hepatocellular carcinoma (HCC) is one of the most common malignant tumors in the world,[1] with high morbidity and mortality. Surgical resection, liver transplantation and physical ablation have been the traditional aggressive treatments for early-stage HCC, which can significantly improve the survival of HCC patients. Physical thermal ablation has been widely utilized in treating HCC because of its advantages of simple operation, less harm to the body and multiple therapy sessions. However, microwave, laser and radiofrequency therapeutic methods (1) cause uneven tissue heating, (2) lack selectivity in killing tumor cells and (3) make conformal ablation difficult, which limits their clinical efficacy. Furthermore, these modalities always induce a temperature higher than 65 °C, resulting in severe damage to normal cells.[2] Therefore, continuous efforts should still be exerted to develop efficient HCC treatment approaches, as highlighted in tumor management.[3]

Magnetic hyperthermia (MH) is an effective anti-tumor modality. The European Union has authorized MH for treating glioblastoma multiforme.[4-7] Recently, the U.S. Food and Drug Administration has initiated clinical trials to treat prostate[8] and pancreatic[9] cancers. The MH heating mechanism is based on the ability of magnetic particles to demonstrate hysteresis loss under an alternating magnetic field (AMF). Since tumor cells are more sensitive to high temperatures than normal cells, magnetic particles used as a heat source induce tumor apoptosis.[10-12] Contrary to conventional thermal ablation, in which heating is targeted at the tissue level, MH is characterized by magnetic particles as a heat source and the intracellular effects of heating. Based on this, MH possesses the following unique advantages: (1) mild treatment temperature (39–45 °C); (2) uniform heating as particles are localized inside cells; (3) selective tumor cell killing; (4) well-defined biosafety and (5) deep tissue penetration. Undoubtedly, MH is an alternative and effective cancer treatment that deserves more research and enhancement.[13-15] However, the limited heating conversion efficiency inspires the design and synthesis of versatile magnetic materials for improving the performance of MH.

In recent years, iron oxide materials have garnered considerable attention. Although many magnetic materials have been developed for MH, most studies only focus on its preparation methods, enhanced biocompatibility, low coercivity and colloidal stability.[16-18] Most iron oxide nanoparticles require a low thermal conversion efficiency and a high injection dosage (milligram level).[5] Many research efforts has shown the

[a]Laboratory of Resource Biology and Biotechnology in Western China, Ministry of Education, Provincial Key Laboratory of Biotechnology of Shaanxi Province, Northwest University, Xi'an, Shaanxi 710069, China. E-mail: liuxiaoli0108@xjtu.edu.cn

[b]Institute of Smart Biomedical Materials, School of Materials Science and Engineering, Zhejiang Sci-Tech University, Hangzhou 310018, China

[c]Institute of Regenerative and Reconstructive Medicine, Med-X Institute, First Affiliated Hospital of Xi'an Jiaotong University, Xi'an, Shaanxi 710049, China

[d]National Local Joint Engineering Research Center for Precision Surgery & Regenerative Medicine, Shaanxi Provincial Center for Regenerative Medicine and Surgical Engineering, First Affiliated Hospital of Xi'an Jiaotong University, Xi'an, Shaanxi 710061, China

† Electronic supplementary information (ESI) available. See DOI: https://doi.org/10.1039/d3ra01294h

maximum specific absorption rate (SAR) value of ferric oxide particles with different sizes (7.6–416 nm) in the diplomatic magnetic field (80 kHz, 32.5 kA m^{-1}) is 75.6 W g^{-1}. And the SAR value decrease with the increase of particle size.[19,20] It usually used template[21] or etching method[22] for fabrication of porous materials, however, the reaction process was complex and poorly controllable. Interestingly, researchers achieved iron oxide microparticles possessing high magnetic permeability, high saturation magnetization and low coercivity[23] by designing their chemical components and modulating their size[24] and shape,[25] which have the potential to significantly improve heating conversion efficiency.[26,27]

In this study, rugby ball-shaped magnetic microcapsules with superior heating conversion efficiency were prepared for MH-triggered cancer treatment. The 'hydrothermal and reduction' method prepared microcapsules resembling rugby balls by adding inorganic salt to Fe^{3+} as a reaction precursor in a closed reactor while controlling the reaction time and temperature. Controlling the reaction parameters to modify the pore size and volume enabled a comprehensive investigation of the structural optimization of microcapsules for MH applications. The optimal magnetic microcapsules possessed a high SAR value and low coercivity, demonstrating a significant heating-generation capacity when exposed to AMF. When synthesized magnetic microcapsules were employed for *in vivo* anti-tumor treatment, the performance of magnetic agents in relieving HCC was achieved.

2. Experimental

2.1 Synthesis of magnetic particles

The ellipsoidal magnetic microcapsules were synthesized by hydrothermal growth of ellipsoidal hematite (α-Fe$_2$O$_3$) microcapsules and then used a gas reduction process to convert α-Fe$_2$O$_3$ into the other phase. The α-Fe$_2$O$_3$ microcapsules were synthesized by hydrothermally treating 3.0 mL of aqueous FeCl$_3$ solution (0.5 M) and 0.72 mL of aqueous NH$_4$H$_2$PO$_4$ (0.02 M) solution at 220 °C for different times. Distilled water was added to a final volume of 40 mL. After stirring for 10 min, the mixture was transferred into a Teflon hydrothermal reaction kettle with a capacity of 50 mL for hydrothermal treatment at 220 °C. The autoclave was naturally cooled down to room temperature about 25 °C. The precipitate was collected by centrifugation, washed with anhydrous ethanol and de-ionized water and dried under vacuum at 60 °C.

Then, 100 mg of α-Fe$_2$O$_3$ microcapsules were annealed in a horizontal quartz tube furnace at 430 °C, 450 °C and 500 °C under a constant flow of 5% H$_2$/95% Ar for 120 min, respectively. The tube furnace was cooled to room temperature while maintaining the same gas atmosphere.

Microcapsules after reduction was coated with oleic acid. 30 mg microcapsules, 10 g octadecene and 0.4 mL oleic acid were mixed and heated to 280 °C for 50 min in argon environment. After the temperature of reaction system dropped to room temperature, anhydrous ethanol was added to the system, and then centrifuged at 8000 rpm min^{-1} for 10 min. The sediment was retrieved, and then it was washed three times with hexane

and anhydrous ethanol. In order to better use in a physical environment, we convert the oil phase microcapsules into water phase by dopamine. 30 mg wrapped in oleic acid, 4 mL tetrahydrofuran and 200 mg dopamine were mixed and heated to 60 °C for 6 h in argon environment. After the completion of reaction, the tetrahydrofuran was volatilized and cleaned to obtain a completely dry microcapsules powder. The dried particles were then dispersed in water.

2.2 Characterization of magnetic microcapsules

The crystal phase of magnetic microcapsules was verified by X-ray diffraction (XRD, Bruker D8 Advanced Diffractometer System). The morphology and size of the microcapsules were observed *via* transmission electron microscopy (TEM, FEI Tecnai F30) and scanning electron microscopy (SEM, S-570, Hitachi). X-ray photoelectron spectroscopy (XPS) measurement was performed using a PHI-5000 VersaProbe III XPS (ULVAC-PHI, Inc., Japan) with Al Kα X-ray radiation as the X-ray source. The magnetic properties of magnetic microcapsules were characterized using a vibrating sample magnetometer (VSM, Beijing Xinke Technology Developments Co., Ltd.).

2.3 Measurement of SAR value

Magnetic microcapsules with 0.2 mg mL^{-1} Fe were placed in a 1.5 mL EP tube and inserted in a water-cooled magnetic induction coil. A fibre probe (SPG-10AB-II) connected to a computer was used to monitor the real-time temperature. The SAR value was calculated using the following equation:

$$\mathrm{SAR} = C\frac{\Delta T}{\Delta t}\frac{1}{m_{\mathrm{Fe}}}$$

where C is the specific heat capacity of agarose gel, $\Delta T/\Delta t$ is the initial slope of the temperature *vs.* time dependence, and m_{Fe} is the weight fraction of Fe.

2.4 Pore analysis

The surface area of magnetic microcapsules was measured by the Brunauer–Emmett–Teller (BET) method, followed analyzed by Tristar II 3020 for the absorption of nitrogen. The pore size and volume of microcapsules were calculated using the BJH method.

2.5 Cell culture

Mouse H22 hepatoma cells were supplied by the American type culture collection and cultured in RPMI 1640 complete media (Gibco, Carlsbad, CA, USA) supplemented with 10% (v/v) heat-inactivated fetal bovine serum (Biological Industries, USA) and 100 U mL^{-1} penicillin–streptomycin solutions (Hyclone Laboratories Inc., USA) at 37 °C in a humidified atmosphere containing 5% CO$_2$.

2.6 *In vitro* cell cytotoxicity

The Fe ion concentration was determined using ICP-MS. The 100 μL per well H22 cells suspension (1 × 10^4 cells per well) was inoculated into a 96-well plate for culturing another 24 h.

Different concentration of magnetic microcapsules suspension (10, 20, 30, 40, 50, 75, 100 $\mu g\ mL^{-1}$) were added to each well, and the cells were incubated for 8 h. To remove excess suspension material, cells were washed by PBS. Cell viability was determined by CCK-8, and the absorbance was measured at 570 nm by microplate reader (Thermo Fisher Scientific, Wilmington, DE, USA).

2.7 H22 tumor-bearing mice model

Six-week-old female BALB/c mice were purchased from Beijing Vital River Laboratory Animal Technology Co., Ltd. (Beijing, China). The Animal Care and Use Committee of Northwest University approved the animal experiment protocols and complied with all relevant ethical regulations. H22 cells (5×10^5 cells per mice) were subcutaneously inoculated at the back of BALB/c mice (right side) to establish the subcutaneous H22 tumor model. When the tumor volumes reached approximately 100 mm^3, mice were randomly divided into four groups: PBS (isotype control), microcapsules only, AMF only and microcapsules plus AMF (seven mice for each group). Tumor-bearing mice were subjected to one injection of microcapsules (0.1 mg of Fe per cm^3) and three AMF treatments on days 1, 3 and 5. The mice were anaesthetized with 2% (v/v) isoflurane and then exposed to an AMF with a frequency of 365 kHz for 10 min. The tumor volume was calculated by the equation (length × width^2)/2.

All animal experimental protocols were reviewed and approved by the Animal Care and Use Committee of the Institute of Process Engineering, Northwest University, and they complied with all relevant ethical regulations.

3. Result and discussion

3.1 Synthesis and characterization of α-Fe$_2$O$_3$ microcapsules

The magnetic microcapsules resembling rugby balls were synthesized using the hydrothermal and reduction method. The hematite (α-Fe$_2$O$_3$) microcapsules were prepared and then thermally reduced to produce Fe$_3$O$_4$ or iron-containing microparticles. The morphology of α-Fe$_2$O$_3$ microcapsules with different reaction times at 220 °C was observed *via* SEM. As shown in Fig. 1a–c, the size of the obtained α-Fe$_2$O$_3$ microcapsules did not significantly change during the prolonged reaction time. However, numerous pores appeared on the surface of α-Fe$_2$O$_3$ microcapsules at 60 h, and the pores were glaring. The surface area of α-Fe$_2$O$_3$ microcapsule was calculated according to the BET, and pore size were measured using the BJH method. As shown in Fig. 1d, the BET surface area reached 23 $m^2\ g^{-1}$ under a reaction time of 0.5 h, which could be due to the various minute particles maintained in the mixture for inadequate reaction times. After that, remarkably, the specific surface area of the microcapsule generally increased within 10 h and reached its maximum when the reaction time was prolonged to 60 h. The pore size of the α-Fe$_2$O$_3$ microcapsules increased in a similar trend as the reaction time increased (Fig. 1e).

The α-Fe$_2$O$_3$ microcapsules prepared under 220 °C for 60 h showed uniform elliptical spherical shape and size distribution, suggesting good experimental reproducibility (Fig. 1f). The XRD
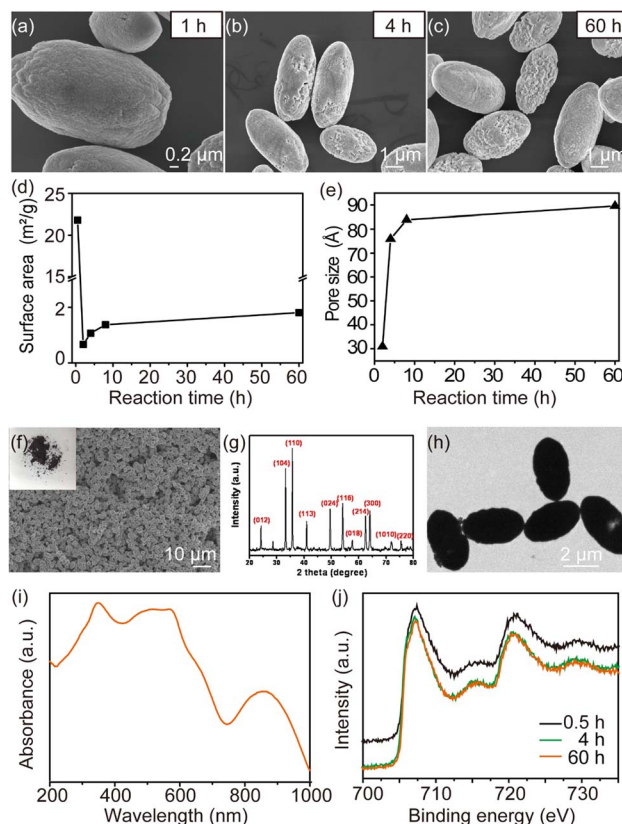

Fig. 1 SEM images of the α-Fe$_2$O$_3$ microcapsules after different reaction times at 220 °C for (a) 1 h, (b) 4 h and (c) 60 h. (d) BET surface area and (e) pore size of the α-Fe$_2$O$_3$ microcapsules with different reaction times. (f) SEM image under low magnification of the α-Fe$_2$O$_3$ microcapsules with a photograph of α-Fe$_2$O$_3$ powder positioned in the upper-left corner. (g) XRD pattern, (h) TEM image, (i) UV absorption spectra and (j) Fe 2p spectra of α-Fe$_2$O$_3$ microcapsules fabricated at 220 °C for 60 h.

results showed that the synthesized α-Fe$_2$O$_3$ microcapsules exclusively corresponded to the trigonal α-Fe$_2$O$_3$ (JCPDS 87-1165), and no other impurity peak was observed (Fig. 1g). Particularly, TEM images showed the obtained microcapsule had a rugby ball-shaped pattern with ~2 μm in width and ~3 μm in length (Fig. 1h), respectively. It was also observed that the aspect ratio of microcapsules resembling rugby balls was approximately 1.5.

As shown in Fig. 1i, compared with the superparamagnetic iron oxide (Fig. S1†), α-Fe$_2$O$_3$ microcapsules had the absorption at 860 nm. The samples were characterized using XPS to further verify the Fe element valence state of the obtained α-Fe$_2$O$_3$ species. The high-resolution Fe 2p spectra showed that two peaks at 724 eV (Fe 2p$_{1/2}$) and 710 eV (Fe 2p$_{3/2}$) were assigned to a Fe^{3+} species (Fig. 1j), which was consistent with the previous report.[28–30]

3.2 Characterization of magnetic microcapsules after reduction of α-Fe$_2$O$_3$ microcapsule

The XRD patterns of the prepared microcapsules under different reduction temperatures are shown in Fig. 2a. Clearly,
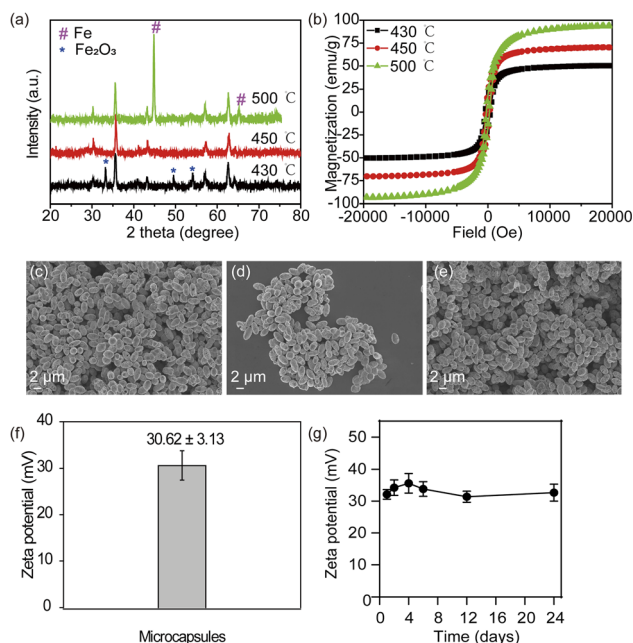
Fig. 2 (a) XRD of the microcapsules after the reduction with different temperatures (430 °C, 450 °C and 500 °C). (b) Hysteresis loop of the microcapsules at 300 K after the reduction with different temperatures (430 °C, 450 °C and 500 °C). SEM image of microcapsules with different reduction temperatures (c) 430 °C, (d) 450 °C and (e) 500 °C. (f) Zeta potential of magnetic microcapsules in solution. (g) Zeta potential measured as a function of time upon incubation in solution.

the reduction temperature would have a significant impact on the formation of the final products. The Fe and Fe_3O_4 appeared when the reduction temperature was between 430 °C and 500 °C. At 450 °C, all of the diffraction peaks can be exclusively indexed as the cubic inverse spinel Fe_3O_4 (JCPDS no. 19-0629), and no other impurities were observed. Therefore, we propose that the composition-controlled synthesis of microcapsules could be achieved by adjusting the reduction temperature.

Next, the morphology of microcapsules at various reduction temperatures was examined using SEM. As the SEM images are shown in Fig. 2c, all the porous microcapsules were uniform in their rugby ball shape. The large-scale microcapsules were observed clearly with uneven and rough surfaces at reduction temperature of 430 °C. When the reduction temperature increased to 450 °C, the high-magnification SEM image of the microcapsules showed that the size of the microcapsules was uniform and well dispersed, with an average width of ~2 and ~3 μm for length (Fig. 2d). Interestingly, the micropores appeared on the surface of the microcapsules and became noticeably rougher when the reduction temperature was changed to 500 °C (Fig. 2e). However, the morphology of microcapsules was not significantly changed.

The magnetic hysteresis loop of microcapsules was characterized using a VSM in order to examine the underlying relationship between the magnetic properties and the reduction temperature. As shown in Fig. 2b, the highest saturation magnetization (M_s) was recorded at ~94 emu g^{-1} under the 500 °C reduction temperature. And microcapsules magnetized

from 1500 to −1500 Oe, which lead to magnetic field energy loss and heat generation by hysteresis (Fig. S2†). Meanwhile, as the temperature was reduced, the M_s of microcapsules increased while the coercivity decreased (Table 1). As the M_s is the dominant factor for higher magnetic heating generation, the magnetic microcapsules synthesized under a 500 °C reduction temperature were chosen for the following experiments.

The zeta potential of magnetic microcapsules is 30.62 ± 3.13 mV (Fig. 2f), which suggested the successful surface modification. Fig. 2g showed that the zeta potential of the magnetic microcapsules did not change for 24 days, indicating the good colloidal stability of the magnetic microcapsules.

3.3 Magnetic hyperthermia properties of magnetic microcapsules

To evaluate the heat induction capability of magnetic microcapsules under AMF, the temperature of magnetic microcapsules dispersed in agarose gel was monitored using an induction heating system. Briefly, 1 mL of magnetic microcapsules with a concentration of 0.2 mg mL^{-1} [Fe] were subjected to AMF with a frequency fixed at 365 kHz and an amplitude varying from 20 to 50 kA m^{-1}. As shown in Fig. 3a, the temperature of magnetic microcapsules increased rapidly at different amplitudes. When the amplitude was set to 50 kA m^{-1}, the temperature of the microcapsules could reach above 47 °C within 30 s. The calculated SAR of magnetic microcapsules based on temperature–time curves is shown in Fig. 3b. The larger SAR value can be detected with the higher amplitude of AMF. The largest SAR value of magnetic microcapsules was obtained for 2391 W g^{-1} with a Fe concentration of 0.2 mg mL^{-1} under AMF (365 kHz, 50 kA m^{-1}), which is more significantly higher than the reported previously. These results indicated that magnetic microcapsules possessed an attractive magnetic heating generation ability.

We utilized H22 cells to evaluate whether magnetic microcapsules induced concentration-dependent cytotoxicity (Fig. 3c). After H22 cells being incubated with microcapsules at different Fe concentration, it was found that the cell viabilities of H22 was above 85% from 5 to 50 μg mL^{-1} of Fe concentration, which indicated that cytotoxicity below 50 μg mL^{-1} is negligible. Quantitative study of cellular uptake at a dosage of 50 μg mL^{-1} showed that the maximum accumulation of magnetic microcapsules occurred at a co-incubation time of 8 h, which could be the optimal time for cell hyperthermia (Fig. S3†). As shown in Fig. 3d, after co-incubation with 50 μg mL^{-1} microcapsules for 12 h, and cells exposed to different magnetic field intensity for 10 min, it showed magnetic field

Table 1 The M_s and coercivity of the magnetic microcapsules with different temperature reductions (430 °C, 450 °C and 500 °C)

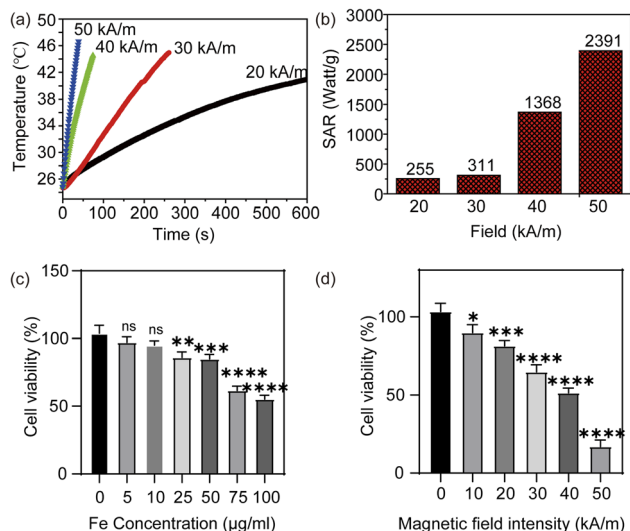| Reduction temperature	M_s (emu g^{-1})	Coercivity (Oe)
430 °C	50	419
450 °C	70	324
500 °C	94	241

Fig. 3 (a) Temperature *versus* time graphs and (b) SAR of magnetic microcapsules under different field intensities. (c) Cell viability of H22 exposed to magnetic microcapsules. $5-100$ μg mL^{-1} concentration of Fe incubated with H22 for 24 h. (d) Cell viability of H22 cells subjected to magnetic microcapsules mediated hyperthermia under different magnetic field intensity. The frequency was 365 kHz.

intensity-dependent cell death trends. At a magnetic field intensity of 40 kA m^{-1}, the cell viabilities decreased to $\sim$48%.

3.4 Antitumor efficacy of magnetic microcapsule-mediated magnetic hyperthermia in hepatoma H22-bearing mice

Magnetic microcapsules with high SAR values can be used for many applications. To investigate the potential of magnetic microcapsules to induce a magnetic hyperthermia-mediated anti-tumor effect, *in vivo* experiments were performed on H22 tumor-bearing mice. In several experimental groups ($n = 7$), H22 cancer cells were xenografted onto the back of BALB/c mice
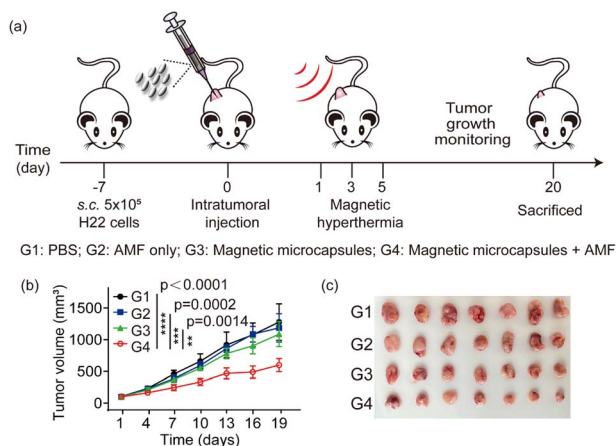

Fig. 4 (a) Schematic illustration of experimental design. (b) Tumor images from each group after the animals were sacrificed. (c) H22 tumor growth curves after different treatment. The error bars represent the means $\pm$ SD. Differences among groups are determined using one-way ANOVA analysis **$p < 0.01$, ***$p < 0.001$, ****$p < 0.0001$.

(right side). Magnetic microcapsules were injected subcutaneously into the tumor (100 mm^3). The mouse was placed in a water-cooled magnetic induction coil. An a.c. magnetic field of 365 kHz at 40 kA m^{-1} was applied for 10 min. The experimental design for the animal is shown in Fig. 4a. Following treatment, the tumor burden was monitored for up to 20 days. For the untreated control group of mice, tumor size increased 3-fold by day 19 (Fig. 4b). The mice treated with either AMF or magnetic microcapsules showed growth behaviors similar to the untreated control. However, for the group that received the hyperthermia treatment with magnetic microcapsule nanoparticles, the tumor growth was delayed during the same period. We also photographed the tumor tissues at the end of treatment (Fig. 4c), which visually confirmed that magnetic microcapsule plus AMF was most effective in suppressing tumor growth.

4. Conclusions

We have successfully constructed a magnetic microcapsule resembling a rugby ball with high M_s and magnetic thermal conversion properties. The composition and morphology of microcapsules could be accurately controlled by controlling the reaction time and temperature, demonstrating superior dispersibility and dimensional homogeneity. As a customized magnetic induction hyperthermia agent for tumor treatment, magnetic microcapsules resembling rugby balls obtained a well-defined heating generation efficiency. In an *in vivo* experiment, microcapsules induced an efficient hepatocellular carcinoma inhibition effect, indicating magnetic microcapsules could be used as a promising magnetic hyperthermia agent. Therefore, our synthetic rugby ball-shaped magnetic microcapsules provide an alternative agent for future biological applications.

Ethical statement

All animal procedures were performed in accordance with the Guidelines for Care and Use of Laboratory Animals of Northwest University and approved by the Animal Ethics Committee of Northwest University. And we declare all experiments were performed in compliance with relevant laws or guidelines and all experiments followed institutional guidelines.

Conflicts of interest

There are no conflicts to declare.

Acknowledgements

References

1 H. Sung, J. Ferlay, R. L. Siegel, M. Laversanne, I. Soerjomataram, A. Jemal and F. Bray, *Ca-Cancer J. Clin.*, 2021, **71**, 209–249.

2 S. L. Liauw, P. P. Connell and R. R. Weichselbaum, *Sci. Transl. Med.*, 2013, **5**, 1–32.

3 T. Hehr, R. Wust, M. Bamberg and W. Budach, *Onkologie*, 2003, **26**, 295–302.

4 M. Johannsen, U. Gneveckow, K. Taymoorian, B. Thiesen, N. Waldofner, R. Scholz, K. Jung, A. Jordan, P. Wust and S. A. Loening, *Int. J. Hyperthermia*, 2007, **23**, 315–323.

5 K. Maier-Hauff, F. Ulrich, D. Nestler, H. Niehoff, P. Wust, B. Thiesen, H. Orawa, V. Budach and A. Jordan, *J. Neuro-Oncol.*, 2011, **103**, 317–324.

6 R. T. Gordon, J. R. Hines and D. Gordon, *Med. Hypotheses*, 1979, **5**, 83–102.

7 A. Jordan, P. Wust, R. Scholz, B. Tesche, H. Fahling, T. Mitrovics, T. Vogl, J. Cervos-Navarro and R. Felix, *Int. J. Hyperthermia*, 1996, **12**, 705–722.

8 K. Mahmoudi, A. Bouras, D. Bozec, R. Ivkov and C. Hadjipanayis, *Int. J. Hyperthermia*, 2018, **34**, 1316–1328.

9 S. V. Spirou, M. Basini, A. Lascialfari, C. Sangregorio and C. Innocenti, *Nanomaterials*, 2018, **8**, 1–22.

10 X. L. Liu, Y. Yang, C. T. Ng, L. Y. Zhao, Y. Zhang, B. H. Bay, H. M. Fan and J. Ding, *Adv. Mater.*, 2015, **27**, 1939–1944.

11 P. G. Dai, W. J. Zhu, B. Yan, Y. Q. Miao, S. S. Hu, X. Gao, X. L. Liu, Y. F. Zhang, G. L. Li, T. B. Zhang, H. Zhang and H. M. Fan, *Adv. Ther.*, 2021, **4**, 200291.

12 B. Hildebrandt, P. Wust, O. Ahlers, A. Dieing, G. Sreenivasa, T. Kerner, R. Felix and H. Riess, *Crit. Rev. Oncol. Hematol.*, 2002, **43**, 33–56.

13 A. Hervault and N. T. K. Thanh, *Nanoscale*, 2014, **6**, 11553–11573.

14 J. Pan, Y. Xu, Q. Wu, P. Hu and J. Shi, *J. Am. Chem. Soc.*, 2021, **143**, 8116–8128.

15 E. A. Perigo, G. Hemery, O. Sandre, D. Ortega, E. Garaio, F. Plazaola and F. J. Teran, *Appl. Phys. Rev.*, 2015, **2**, 041302.

16 R. Hergt, S. Dutz and M. Roder, *J. Phys.: Condens. Matter*, 2008, **20**, 385214.

17 S. Laurent, S. Dutz, U. O. Hafeli and M. Mahmoudi, *Adv. Colloid Interface Sci.*, 2011, **166**, 8–23.

18 J. Dulinska-Litewka, A. Lazarczyk, P. Halubiec, O. Szafranski, K. Karnas and A. Karewicz, *Materials*, 2019, **12**, 12040617.

19 M. Ma, Y. Wu, J. Zhou, Y. Sun, Y. Zhang and N. Gu, *J. Magn. Magn. Mater.*, 2004, **268**, 33–39.

20 T. Hosono, H. Takahashi, Y. Sato, K. Tohji and B. Jeyadevan, *AIP Conf. Proc.*, 2007, **898**, 135–138.

21 L. Wang, D. Z. Ni, D. Yang, K. B. Zhou and S. Yang, *Chem. Lett.*, 2010, **39**, 451–453.

22 Y. Q. Shen, F. Zhang, P. F. Song, Y. C. Zhang, T. Zhang, X. Q. Wen, J. Q. Ma, D. Zhang and X. Y. Du, *J. Alloys Compd.*, 2022, **903**, 163971.

23 S. K. Boda, A. V. Anupama, B. Basu and B. Sahoo, *J. Phys. Chem. C*, 2015, **119**, 6539–6555.

24 A. A. Taheri and M. Taghilou, *Int. J. Eng.*, 2021, **34**, 263–271.

25 H. X. Gao, T. B. Zhang, Y. F. Zhang, Y. M. Chen, B. Liu, J. P. Wu, X. L. Liu, Y. D. Li, M. L. Peng, Y. Zhang, G. Xie, F. Q. Zhao and H. M. Fan, *J. Mater. Chem. B*, 2020, **8**, 515–522.

26 L. Lai, H. Zhou and B. Lai, *Chem. Eng. J.*, 2018, **349**, 633–645.

27 J. Li, J. Yan, G. Yao, Y. Zhang, X. Li and B. Lai, *Chem. Eng. J.*, 2019, **361**, 1317–1332.

28 Y. Wang, C. Xie, D. Liu, X. Huang, J. Huo and S. Wang, *ACS Appl. Mater. Interfaces*, 2016, **8**, 18652–18657.

29 D. Li, J. Zhou, X. Chen and H. Song, *ACS Appl. Mater. Interfaces*, 2016, **8**, 30899–30907.

30 Z. Yu, H. Li, J. Lu, X. Zhang, N. Liu and X. Zhang, *Electrochim. Acta*, 2015, **158**, 264–270.